Trapping hydrogen: Confined catalysis for improved hydrogen borrowing selectivity

Julio C. S. Terra,[a] Jackson DeWolfe,[a] Jesus A. Valdez,[b] Audrey Moores[a, c, *]

a Centre in Green Chemistry and Catalysis, Department of Chemistry, McGill University, 801 Sherbrooke St. West, Montreal, QC, H3A 0B8, Canada

b Facility for Electron Microscopy Research (FEMR), McGill University, Montréal, Québec, Canada

c Department of Materials Engineering, McGill University, 3610 University Street, Montreal, Quebec H3A 0C5, Canada

KEYWORDS confinement effects, alcohol amination, hydrogen borrowing, ruthenium, alumina, silica, yolk-shell

ABSTRACT: Alcohol amination via hydrogen borrowing is an established method for the clean and simple alkylation of amines with alcohols, which are stable and available in bulk; it also does not require the addition of hydrogen to reduce the imines or the use of coupling agents. A common problem however in those systems is the need to employ additives to prevent stagnation of the product at the imine stage, which indicates inefficient usage of the borrowed hydrogen atoms. In this work, we designed a catalyst series to demonstrate that confined environments can assist with improved selectivity. To this end, we encapsulated Al_2O_3/$Ru(OH)_x$ nanocatalysts inside mesoporous silica in a yolk-shell architecture and were able to trap the hydrogens to increase the amine yield from 12% to 82%, with a 3-fold increase in selectivity without the need of any additive; we found the presence of mesopores in the silica shells to be essential to enable access to the catalytic sites and the yolk-shell gap size to be the key parameter influencing the reactivity of the catalytic system. To the best of our knowledge, this is the first report of a confined hydrogen borrowing reaction, an approach that can be extended to the other types of cascade reactions that produce labile intermediates.

Introduction

Hydrogenations are present in at least a quarter of all chemical processes.[1] They can happen either through direct hydrogenation, when H_2 is the source of hydrogen atoms; or through transfer hydrogenation, when the hydrogen atoms come from a non-H_2 source.[2] The latter process, although less atom economical, has the advantage of not relying on hazardous pressurized hydrogen gas.[3] A unique type of hydrogen transfer happens when the hydrogen source does not only donate hydrogen atoms but is also involved in an intermediate reaction within the cycle. The *in-situ* formed intermediate can then be hydrogenated in a following step, as it happens in the alcohol amination process (Scheme 1). First, the catalyst oxidizes an alcohol molecule, "borrowing" two hydrogen atoms. The alcohol, now activated as a carbonyl, condenses with an amine or ammonia to form the corresponding imine. Lastly, the catalyst returns the hydrogens to reduce the imine, forming a substituted amine. This is a typical hydrogen borrowing process, also known as hydrogen auto-transfer.[4, 5] Alcohol amination is particularly interesting because it gives access to substituted amines from alcohols, which are stable, available, and possibly bio-sourced.[6]

An effective hydrogen borrowing catalyst needs to both withdraw and return the hydrogen atoms within the catalytic cycle, so the same system is bound to perform the antagonistic tasks of dehydrogenation and hydrogenation. The first catalysts for alcohol amination were published in 1981 by Grigg *et al.*, using Rh and Ir triphenylphosphine complexes,[7] and by Watanabe and co-workers, using a Ru triphenylphosphine coordination compound.[8] Although there are now systems in the literature based on abundant metals,[9] Ru and Ir catalysts still dominate the alcohol amination literature.[6]

Scheme 1. Amination of alcohols through the hydrogen borrowing mechanism.

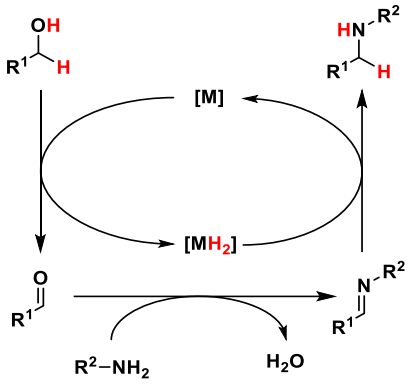

Many alcohol amination catalytic systems are assisted by base additives. Fujita *et al.* for instance reported a $[Cp^*IrCl_2]_2$/K_2CO_3 system that could quantitatively catalyze the coupling of aniline and benzyl alcohol to give the secondary amine (Entry 1, Table 1).[10] The Crabtree and Eisestein groups performed Density Function Theory (DFT) studies on Fujita's system and found the central role of carbonate as a

Table 1. Alcohol amination conditions from the literature for the coupling of aniline (1) and benzyl alcohol (2).

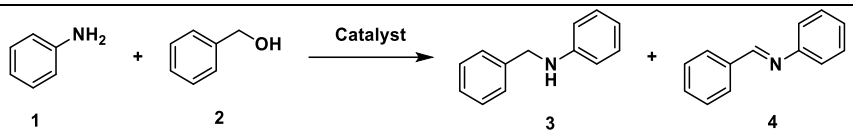

1 2 3 4

Entry	Ref.	Catalyst	Load (mol%)[a]	Time (h)	Temp. (°C)	Additives	Conv. (%)[b]	Selectivity of **3** (%)
1	10	$[Cp^*IrCl_2]_2$	5	17	110	K_2CO_3 5 mol%[a]	100	100
2	12	Ru/N-doped carbon	0.3	24	130	KOH 50 mol%[a]	96	100
3	14	$Ru(OH)_x/Al_2O_3$	5	11	132	none	99	90
4	15	$(Ni_{0.5}Cu_{0.5})Fe_2O_4$	10	1[c]	240	iPrOH[d]	75	99

[a] mol% of **1**; [b] based on **1**; [c] under microwave radiation; [d] 10% of total solvent volume.

ligand that accepts a hydride in the alcohol oxidation step, and then returns it to reduce the imine.[11] They found that, although the catalyst has the challenging task of performing the two mirroring reactions, the overall process moves forward effectively for two main reasons: 1) alcohol dehydrogenation via proton transfer followed by β-hydride elimination is preferred over amine oxidation, and 2) the imine is more easily hydrogenated than the aldehyde. The authors also found that the catalyst is not involved in the carbonyl-amine condensation step. The Lang group published an interesting study on a solid catalyst made by pyrolyzing carbon power loaded with cis-$Ru(phen)_2Cl_2$, which formed Ru NPs supported on N-doped carbon.[12] The authors reacted aniline **1** and benzyl alcohol **2** to obtain full selectivity to the secondary amine **3** using KOH as an auxiliary base (Entry 2, Table 1). When NaOH was used as the base, the system gave full selectivity to the corresponding imine **4**. Lang *et coll.* related this phenomenon to the larger radius of K^+, which could coordinate to the C=N bond on the imine and elongate it, facilitating the hydrogenation step. Using this catalyst based on Ru NPs on N-doped carbon and switching the base between KOH and NaOH, the authors were able to tune the reactivity using several substrates to give either the amine, through the full hydrogen auto-transfer mechanism, or the imine, through what they called the acceptorless hydrogenation coupling reaction.

The use of auxiliaries is however a drawback in the context of Green Chemistry, especially toxic ones like strong inorganic bases. It goes against atom economy (principle 2), as well as principles 3 and 5 which call for less hazardous syntheses and the use of benign auxiliaries.[13] A very robust auxiliary-free heterogeneous system for alcohol amination is the one developed by the Mizuno group, based on $Ru(OH)_x$ deposited on alumina (Entry 3, Table 1);[14] the authors obtained 90% selectivity to the secondary amine **3** in the reaction of aniline **1** and benzyl alcohol **2**, having the corresponding imine **4** as the sole by-product. Also in the absence of an additional base, our group has catalyzed the alcohol amination reaction with plasma-made Ni/Cu mixed ferrite nanoparticles (Entry 4, Table 1).[15] Although no base was added to the system, the addition of isopropanol as a sacrificial source of hydrogens was essential to improve the selectivity of the system to form the amine, suggesting that stagnation of the cycle at the imine stage might be associated with low availability of hydrogen.

In fact, the proton and the hydride "borrowed" by the catalyst can recombine and form a labile H_2 ligand, which could detach from the metal center and leave the liquid phase as H_2 gas due to its low solubility in organic solvents.[16] The Crabtree group studied a Ru-catalyzed alcohol amination reaction system[17] and found through DFT studies that H_2 release or retention is decisive in the formation of the substituted amine. Such a finding was corroborated by H_2 detection experiments which showed that low amine selectivity was accompanied by the presence of free H_2 in solution.

Cascade reactions such as the N-alkylation of amines with alcohols are indeed challenging processes due to the antagonist tasks given to the catalyst. Mattey *et al*. took a literal approach and compartmentalized the process in a flow system; the oxidation and reduction pathways were carried out separately by different biocatalysts but interconnected in a flow reactor.[18] Another way to compartmentalize incompatible catalytic systems for cascade reactions is to use hierarchical nanostructures, which can work as multicomponent nanoreactors.[19] These nanoreactors can also induce the retention of intermediates in the proximity of catalytic centers, a strategy that can as well be applied to push the completion of cascade reactions.[20] Species confined in nanopores, for instance, have been shown to have slower diffusion rates when compared to the same species in bulk solutions. Such an effect can stem from the similar dimensions of the molecules and the pore openings, which enhances molecule-wall interactions and may even increase the viscosity of confined fluids.[21] Dong *et al.* used single-molecule fluorescence to study the oxidation of amplex red in 2-3 nm wide cylindrical pores and found diffusion rates of intermediates inside the pores to be 5 orders of magnitude lower than the diffusion in the bulk solution.[22] The lower diffusion caused an enrichment of intermediates around the catalytic site, which increased reaction rates. Our group has also worked with catalysis confined in mesopores, more specifically the cascade coupling of an amine, an aldehyde, and an alkyne inside the pores of mesoporous silica MCM-41;[23] the system benefited from the slow diffusion and hence high concentration inside the pores of both released Cu^+ ions and *in-situ* generated intermediates.

Confined reactions have been used in various contexts to make catalytic systems greener and more efficient,[24] but this strategy has not yet been applied to hydrogen borrowing. In this context, here we report for the first time a nanoconfined hydrogen borrowing catalytic system. To the best of our knowledge, we systematically demonstrate for the first time the strategy of trapping a gas intermediate within a nanostructure to improve a cascade reaction system. We created yolk-shell structures by encapsulating nanoparticulated $Ru(OH)_x/Al_2O_3$ in mesoporous silica shells, and applied them as catalysts for alcohol amination. By controlling the mor-

phology of the porous shells and the yolk-shell voids, we were able to tune the selectivity of the system towards the secondary amine without the use of any additive.

Results and Discussion

Our goal was to design a heterogeneous catalyst for the hydrogen borrowing reaction featuring a confined space, hence we were inspired by Mizuno's $Ru(OH)_x/Al_2O_3$ system[14] as a simple and robust core for our design. Commercial spherical alumina NPs (diameter 37.8 ± 25.5 nm, PDI 0.4, Fig. S1) were modified by being dispersed in water with $RuCl_3.3H_2O$ (1 wt% of Ru) and stirred overnight at pH 13.2 (step 1, Fig. 1). The construction of the yolk-shell architecture was based on the methodology reported by Yin and co-workers.[25, 26] The resulting dark gray powder $Ru(OH)_x/Al_2O_3$ was refluxed with PVP (M_w 55,000) to create a sacrificial template layer (step 2, Fig. 1), which was then covered with silica using the Stöber method (step 3, Fig. 1). The silica-coated material was refluxed with PVP (M_w 10,000) to create a second protective layer (step 4, Fig. 1); this second protective layer allowed internal and controlled etching of the silica structure upon treatment with a concentrated NaOH solution (step 5, Fig. 1). Base etching was tested at varied times (2, 3, 4, 5, and 6 h), affording materials $Ru(OH)_x/Al_2O_3@pSiO_2$ E2, E3, E4, E5, and E6. Finally, the catalysts were pyrolyzed at 550 °C (step 6, Fig. 1) to remove template residues, giving materials $Ru(OH)_x/Al_2O_3@pSiO_2$ E2P, E3P, E4P, E5P, and E6P. As a control, we also pyrolyzed the non-etched silica-coated material (skipping step 5 in Fig. 1), providing material E0P.

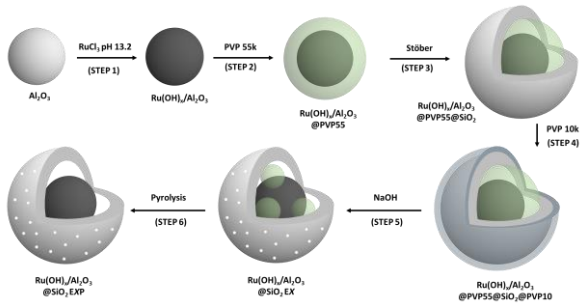

Figure 1. Multi-step procedure for catalyst synthesis.

The duration of the base treatment had a direct impact on the morphology of the silica shells, as evidenced by TEM images (Fig. 2, additional images in Fig. S3). The TEM micrographs were chosen as representatives of the final etched and pyrolyzed materials, showcasing the difference between the non-etched catalyst (material E0P, Fig. 2a, g) and the etched materials (E2P, Fig. 2b-f, h-l). Using commercial Al_2O_3 (diameter 37.8 ± 25.5 nm, PDI 0.4) as the core, we were able to achieve reasonable control over the silica coating and observe clear overall trends. The progressive deterioration of the silica shells is noticeable from the thicker silica coating of on average 32 nm on E2P, which reduces to about 19 nm on E3P, and then to visibly thinner coatings of 9-11 nm after 3 hours of etching (materials E4P, E5P and E6P, more evident on the higher magnification micrographs Fig. 2g-l, detailed thickness measurements in Fig. S4). The progressive deterioration and thinning of the silica shells then evolves to their eventual full dissolution. Analysis of TEM images with 400-600 particles per sample reveal a predominance of coated particles on samples etched for 2-5 h (E2P, E3P, E4P, and E5P present 10-20% uncoated particles), and a predominance of 70% of uncoated particles on material E6P, after 6 hours of etching (Fig. S5). In addition, the silica shells become textured and the void between the yolk and the shell becomes more apparent after 3 hours of etching, as we will discuss further in this text.

The presence of Ru in the materials was confirmed by ICP-OES and XPS (Fig. S6), but particles of Ru metal or oxide could not be consistently identified on TEM micrographs (Fig. S7). This observation implies a high dispersion of Ru species throughout the Al_2O_3 surface, as previously observed by the Mizuno group.[14] Also in accordance with Mizuno's findings, XPS analysis showed consistent Ru $3d_{5/2}$ signals around 281.6 eV, a shift to lower binding energy when compared to the parent material $RuCl_3$ (282.4 eV).[27] No significant shift in the Ru $3d_{5/2}$ signal was observed upon base treatment, confinement, or pyrolysis at 550 °C. The effect of pyrolysis was however noticeable on TGA. Template mass loss of 4-6% was observed on the non-pyrolyzed materials but disappeared on the pyrolyzed catalysts (Fig. S9), proving the effectiveness of the thermal treatment in removing template remnants. The composition and morphology of the nanostructures were also confirmed by

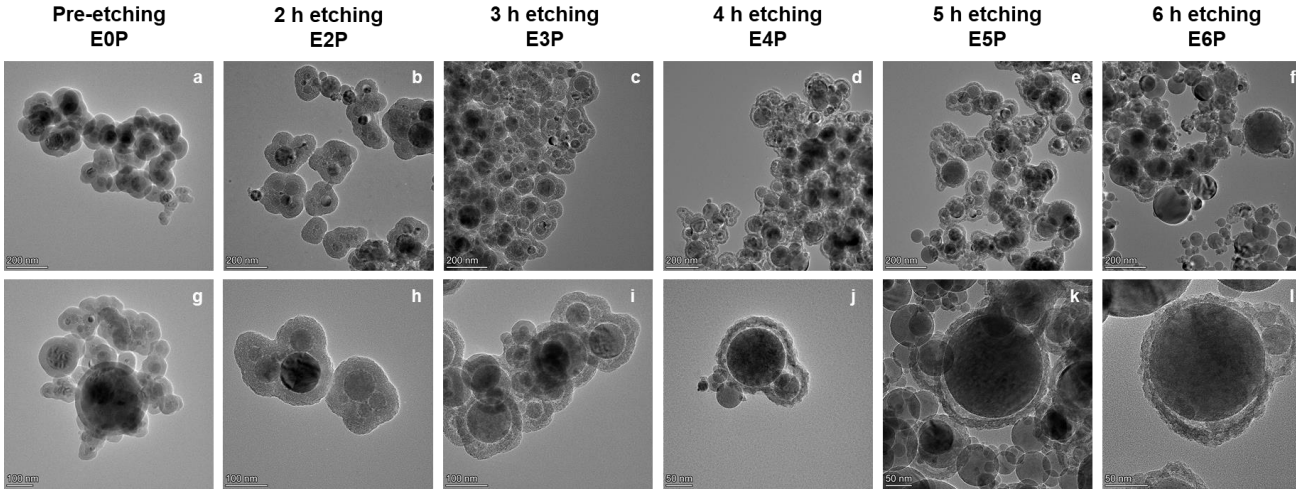

Figure 2. TEM images of the following pyrolyzed catalysts: $Ru(OH)x/Al_2O_3@pSiO_2$ E0P (a, g), E2P (b, h), E3P (c, i), E4P (d, j), E5P (e, k), E6P (f, l).

EDAX elemental mapping and nanotomography experiments. Elemental mapping confirmed that the core was composed of Al and O (Fig. 3b and d) and the shells of Si and O (Fig. 3c and d). The low Ru content (around 1 wt% as measured by ICP-OES for $Al_2O_3/Ru(OH)_x$) challenged the detection limits of the EDAX instrumentation but the dotted white circles indicating the alumina cores from the HAADF image (Fig. 3e) aid in the visualization of the higher density of signal in these regions when compared to noise in the other regions of the micrograph. The image reconstructed by nanotomography (Fig. 4, additional media on section S8) confirms the yolk-shell structure in three dimensions, showcasing the empty gap between the core and the shell and the porous texture of the silica layer.

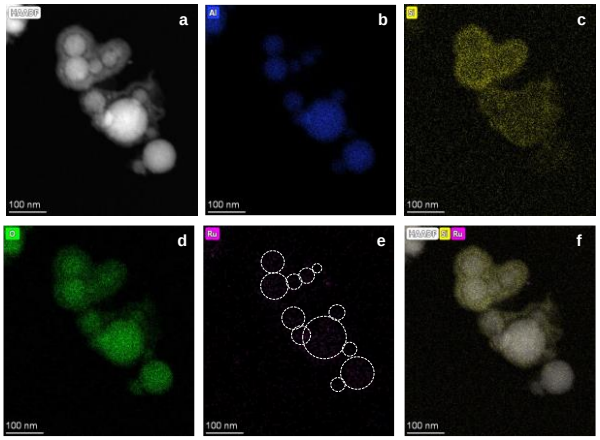

Figure 3. EDAX mapping of material $Ru(OH)_x/Al_2O_3$@$pSiO_2$ E5P: a) HAADF image, b) Al mapping, c) Si mapping, d) O mapping, e) Ru mapping with the contour of alumina cores based on the HAADF image, and f) overlap with the HAADF image with Si and Ru mapping.

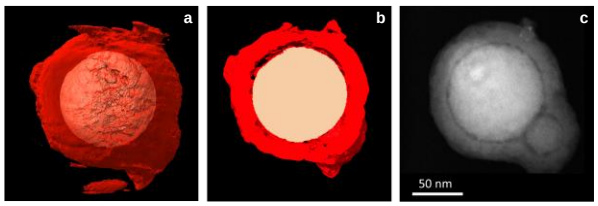

Figure 4. Nanotomography of material $Ru(OH)_x/Al_2O_3$@$pSiO_2$ E5P. The three-dimension image is shown in (a), followed by a two-dimensional intersect image in (b) showcasing the yolk-shell gap. The HAADF image is shown in (c). The three-dimensional rotation video can be found in the supporting information, section S8.

We then studied the ability of the series of produced materials to catalyze the coupling of aniline **1** and benzyl alcohol **2** to produce the corresponding secondary amine **3** (complete alcohol amination mechanism), and the corresponding imine **4** (incomplete alcohol amination, *i.e.* acceptorless hydrogenation). Pure alumina NPs gave 10% yield of imine **4** and no amine **3** (Table S2, entry 2), pure silica NPs produced neither (Table S2, entry 3), and the unconfined catalytic system $Al_2O_3/Ru(OH)_x$ afforded 25% imine **4** and 12% amine **3** (Figure 5)**.** These results suggest that alumina contributes to the dehydrogenation step, which leads to imine formation;

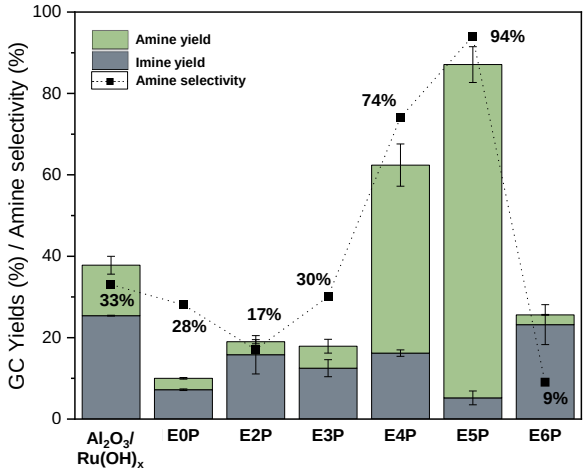

Figure 5. GC yields on amine **3** and imine **4** obtained from the reaction between aniline **1** and benzyl alcohol **2** catalyzed by, from left of right: $Ru(OH)_x/Al_2O_3$ with no silica shell (unconfined), confined and pyrolyzed non-etched material E0P, and confined, catalyzed, and etched (2-6h) materials E2P, E3P, E4P, E5P, and E6P. The dotted line and numbers around the dots represent the selectivity to amine **3**. The only products observed were **3** and **4**. Reaction conditions: 0.25 mmol of aniline, 0.38 mmol of benzyl alcohol, 6 mL of mesitylene, 100 mg of catalyst, 135 °C, 18h, 1 atm of argon. Expanded results on Table S2.

$Ru(OH)_x$ is essential for hydrogenation, which leads to the desired secondary amine; and silica does not play a direct catalytic role in the system, in agreement with the original findings of the Mizuno group.[14] Moving on to the systems catalyzed under confined conditions (results in Fig. 5), we can observe the strong effect of the catalyst's hierarchical structure and morphology. The confined and non-etched material gave lower yields than the unconfined $Ru(OH)_x/Al_2O_3$ system (*i.e.* 7.2% imine and 2.8% amine with E0P). The pyrolyzed and etched catalysts, on the other hand, showed a general trend of increasing yields and selectivities up to a maximum with E5P (5.2% imine and 81.9% amine), followed by a decrease with E6P (23.2% imine and 2.3% amine). The low activity of the non-etched material E0P indicates the importance of opening the porous structures of the shells to give access to the catalytic sites. On the same lines, non-pyrolyzed materials afforded yields of 21-24% of imine **4** and 4-20% of amine **3** (Table S2, entries 12-14), highlighting the importance of the pyrolysis step during the synthesis of the catalysts to expose the catalytic surface and allow the reactions to proceed. The drastic decrease in activity with catalyst E6P, on the other hand, showcases the importance of the presence of porous silica structures, which are mostly destroyed after 6 hours of base treatment.

The intermediate materials E2P, E3P, E4P, and E5P; although all pyrolyzed and etched, bearing open porous structures, and made mostly of silica-coated structures (80-90% of coated particles); still have distinct catalytic behaviours. E2P and E3P are less active than the unconfined system, while E4P and E5P have improved activity when compared to the unconfined system; the latter affording an impressive 94% selectivity to the desired product. Varying the etching time is a strategy that directly affects the morphology of the silica shells, so we

looked deeper at their morphological features to better understand our catalytic systems.

The morphology of the materials was investigated using N_2 adsorption experiments. BET surface areas started at 53 $m^2 g^{-1}$ before any etching (E0P) and steadily increased to a maximum of 196 $m^2 g^{-1}$ after 3 hours of etching (*i.e.* almost a 3-fold increase); after this 3-hour etching threshold, we noticed a gradual decrease in BET surface area up to 137 $m^2 g^{-1}$ after 6 hours of etching (Fig. S10a). Total pore volumes followed the same pattern, initially increasing with etching times, from 0.23 $cm^3 Å^{-1} g^{-1}$ before etching (E0P), reaching a maximum 0.49 $cm^3 Å^{-1} g^{-1}$ after 3 hours of etching (*i.e.* over 100% increase in pore volume), followed by a continuous decrease up to 0.18 $cm^3 Å^{-1} g^{-1}$ after 6 hours of etching (Fig. S10b). The initial increase in BET surface area and total pore volume is related to the opening of the silica structures upon base treatment. Longer etching times however caused a progressive deterioration of the silica shells and eventual complete collapse of the silica structures, as observed in TEM, hence the decrease in surface area and pore volume after 3 hours of base etching. It is interesting to note that the inflection point at 3 hours of etching was exactly the point at which the catalysts changed behaviour.

We also obtained DFT pore size distributions using data from N_2 adsorption experiments (Fig. 6a-e). An important observation is the presence of mesoporosity (2-50 nm) upon etching, which does not exist in the non-etched material E0P (Fig. S13). Moreover, there is a main peak present in all etched samples at 3.8 nm, which we have shaded in light gray and labeled region A in Figure 6. Upon longer etching times, this peak persisted but became narrower, and peaks corresponding to larger mesopores (6-24 nm) progressively developed in the area we shaded in darker gray and labeled region B. In fact, the main peak in region A for E2P and E3P (Figure 6a,b) seems to be composed of an overlap of a taller peak centered at 3.8 nm and shoulder peaks around 4-6 nm. With longer etching times (E4P, E5P, E6P, Figure 6c-e), the main peak was maintained and narrowed while the shoulder peaks shifted to region B in the plots. This movement suggests two types of porosity in our samples: one that was created early in the etching process and remained at 3.8 nm, and another type that was enlarged with progressive etching. In fact, yolk-shell structures are known to present two distinct porosity profiles in the same material: the pores within the shell structure and the yolk-shell voids.

While N_2 adsorption has the advantage of measuring the whole of the sample, it does not discriminate between the pores in the silica shells and the voids between the alumina yolk and the silica shell.[28-30] This discrimination was done through manual measurements of yolk-shell voids in TEM images to obtain the histograms of yolk-shell void size distribution in Figure 6f-j (sample measurements in Fig. S11). As opposed to N_2 adsorption, TEM measurements only represent a fraction of the sample, but we could selectively measure the yolk-shell voids. The analysis of both methods combined gave precious information about the morphology of our catalysts. The histograms built from measuring TEM micrographs (Figure 6f-j) are analogous to the N_2 adsorption plots but only account for yolk-shell voids, excluding the pores inside the silica shells. These plots show an almost exclusive population of region A for E2P and E3P (Fig. 6f, g), and a shift to region B for more etched samples (E4P, E5P, E6P, Fig. 6h-j). This shift of the histograms to region B is consistent with the shift of the shoulder peaks in Figure 6a-e to region B, indicating that those shoulder peaks likely correspond to yolk-shell voids, which became larger with longer etching times. That leaves the taller peak at 3.8 nm for the pores within the silica shells, which are in the same order of magnitude as the observations of Zhang and co-workers for their protected silica-etching protocol.[26] However, contrary to the observations of Zhang *et al*. in their surface-protected SiO_2@void@SiO_2 system, longer base treatment did not cause a noticeable increase in the pore size within the silica shells, but instead it led to an opening of the void size in our surface-protected Al_2O_3@void@SiO_2 system. In our case, the shell porosity was developed up to around 3.8 nm, at which point the base was able to effectively access the interior of the structures and act from the inside out. The 3-hour mark was the limit at which internal etching becomes dominant over etching of the pores in the shells. Larger cavities contribute less to surface area and pore volume, corroborating with the fact that the 3-hour threshold is the inflection point at which pore volume and surface area begin to decrease in our series of materials.

It is interesting to note that the jump in catalytic activity and selectivity happens after the 3-hour etching mark, exactly when the surface area and total pore volumes inflected, and the porosity profile showed the presence of larger yolk-shell voids (region B in Fig. 6). With the more open structures, catalyst E4P brought the amine selectivity up to 74%, more than doubling the 30% observed for its counterpart E3P. Catalyst

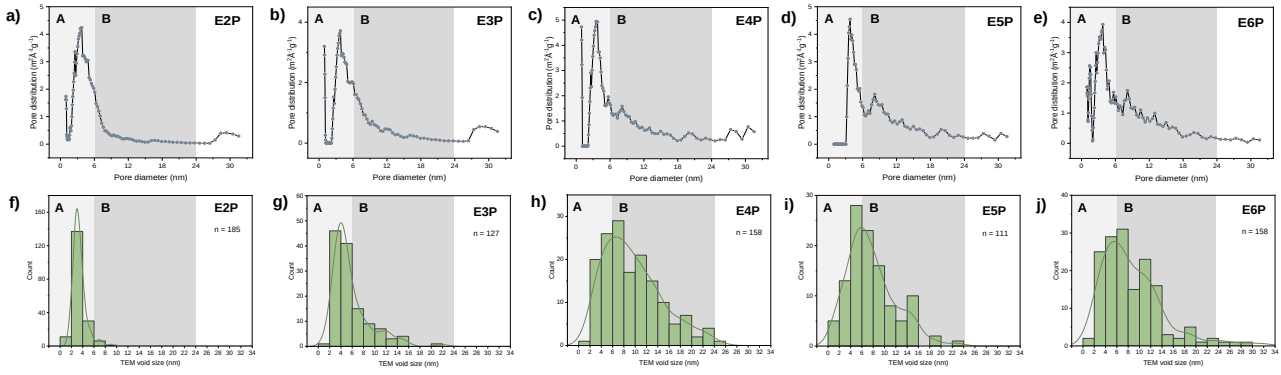

Figure 6. a-e) DFT pore size distribution for the pyrolyzed materials $Ru(OH)_x/Al_2O_3$@$pSiO_2$ E0P (non-etched), E2P, E3P, E4P, E5P, and E6P, in this order, obtained from N_2 adsorption experiments. f-j) yolk-shell gap sizes measured from TEM micrographs of the same pyrolyzed materials $Ru(OH)_x/Al_2O_3$@$pSiO_2$ E0P (non-etched), E2P, E3P, E4P, E5P, and E6P, in this order. The shaded areas A (lighter gray) represents the small mesoporous range that comprises both pores in the silica shells and smaller yolk-shell gaps, while the shaded areas B (darker gray) represent larger mesopores which come mostly from yolk-shell gaps only.

E5P, with even more open voids than E4P, was more efficient and afforded a selectivity of 94% to the complete alcohol amination product. Catalyst E6P, on the other hand, presented low yields and a 10-fold decrease in selectivity when compared to E5P, likely due to the dominance of uncoated particles in that case.

Two factors can influence the success of the hydrogenation step, as highlighted in Scheme 2: 1) the presence of imine molecules in the vicinity of the catalytic site, and 2) the retention of H_2 on the catalyst [MH_2]. The confined nanoreactor system in a mesoporous shell can address both factors. First, slower diffusion out of the system increases the residence time of the imine intermediate in the proximity of the metal. Second, slower diffusion of the labile H_2 ligand out of the confined cage can create a local concentration of H_2 molecules, favouring the reverse reaction in the equilibrium [MH_2] ⇌ [M] + H_2, as highlighted in the expanded catalytic cycle shown in Scheme 2; the stability of the [MH_2] adduct is a key point in driving the reaction towards the formation of the amine.[17]

Scheme 2. Alcohol amination through the hydrogen borrowing mechanism, highlighting the role of H_2 retention.

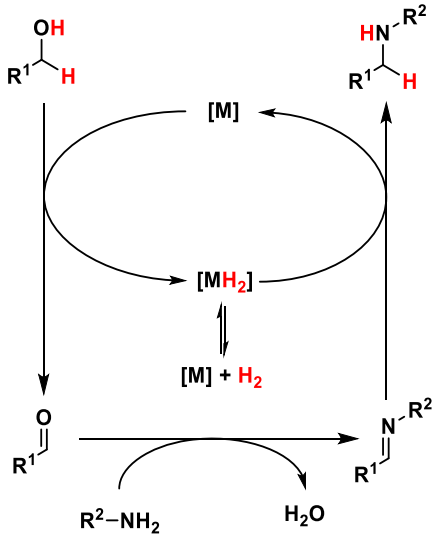

In this context, we decided to investigate the release of H_2 gas in our systems in the presence and absence of the confining silica shell. For that, we removed gas aliquots of the headspace of our sealed reaction vials at the end of the reaction cycle and analyzed this headspace by GC-TCD to look for evidence of the lability of H_2 in two of our systems: one catalyzed by unconfined $Ru(OH)_x/Al_2O_3$, and another one catalyzed by confined E4P. We were able to detect H_2 in the first case, while no H_2 was detected in the latter (Fig. S14). The presence of H_2 in the headspace of the unconfined system corroborated with the findings of the Crabtree group[17] and suggested that the loss of hydrogens atoms is related to low amine selectivity (unconfined $Ru(OH)_x/Al_2O_3$ system). The absence of H_2 in the headspace of the confined reaction suggested that our confined catalyst was effective in trapping the hydrogens, leading to a higher concentration of [MH_2] species in the nanoreactor and, consequently, more successful hydrogenations.

Given such catalytic results, it is clear that the confined yolk-shell structure can drive the reaction to high amine selectivities, and its morphology directly affects the outcome of the reaction. The presence of mesopores in the shells is important to allow access to the catalytic site, as shown by the low conversion of E0P, in which the lack of porosity barred access of the substrates to the catalytic sites. Mesopores may also be responsible for maintaining the hydrogen atoms inside the system as indicated by the H_2 measurements; this concentration effect also applies to the imine intermediate. Nanopores and nanochannels are known to have special diffusion patterns when compared to bulk systems. Due to the enhanced interaction of the diffusion stream with the walls of the porous structure, diffusion rates are greatly influenced by adsorption equilibria (molecule-wall interactions), as well as molecule-molecule interactions which are also enhanced under confined spaces. Microporous systems experience molecule-wall interactions over the entire pore space, while mesoporous systems experience those interactions in the layers surrounding the walls but also contain a central region with bulk diffusion properties, where molecule-wall interactions are limited or inexistent.[31] This mesoporous access to the reacting site can hence play a decisive role in systems like ours which rely on a balanced rate between the retention of intermediates in the catalytic site and the release of fully formed products.

Mesoporosity in the shells is however not enough to secure high conversions and selectivities in our system, as one can observe in the low activities of E2P and E3P (Fig. 5). The higher catalytic activity observed for E4P and E5P happens when larger yolk-shell voids are created in the structures, which in our case takes place after the 3-hour etching threshold as observed in Fig. 6. Thus, in addition to the mesoporous shells, those larger gaps in the 6-24 nm range seem to be a key feature positively affecting reactivity. While the mesoporous shells are responsible for slowing down the diffusion of intermediates, these yolk-shell voids are where the reaction happens; these spaces are the *de facto* nanoreactors, so it is reasonable to expect that their dimensions would powerfully affect reactivity. Our data shows that reaction spaces in the 2-6 nm range (region A in Fig. 6, *i.e.* 80% of the measured voids in E2P and 69% of the voids measured in E3P, *versus* about 30% for E4P, E5P, and E6P) are unfavourable for the completion of the alcohol amination cycle in our system specifically. Given that the substrate molecules have flat dimensions in the 0.5-0.6 nm range and the product molecules have about 1 nm diameter, one can envisage the geometrical restrictions for movement within the nanoreactor. Although the concentration of intermediates in the vicinity of the active sites can improve the catalytic system, reactivity is controlled by an intricate diffusion balance since products also should be able to diffuse away. In this context, yolk-shell voids predominantly in region B of Figure 6, in fact mostly in the 6-16 nm range (56-59% for E4P, E5P, and E6P) were revealed as the ideal nanoreactor dimensions for our system. E6P however behaved much like the unconfined system $Al_2O_3/Ru(OH)_x$, probably due to the high amount of destroyed silica shells. Hence, our results showed that, although the limited diffusion through the mesoporous shells is beneficial for this specific catalytic system, overly tight reaction spaces are detrimental.

Our system followed the so so-called volcano behaviour: low catalytic activity was observed in tight spaces, which increased with the increasing nanospace size until a maximum catalytic activity, which then decayed when the space was too large and approached bulk (unconfined) behaviour. This is a common reactivity pattern in nanoconfined systems.[32, 33]

Conclusions

Confined catalysis is a versatile concept with a wide range of applications. We produced yolk-shell $Al_2O_3/Ru(OH)_x@SiO_2$ structures with porous silica shells and varied yolk-shell gaps through the surface-protected etching methodology. We successfully used those materials to demonstrate the use of confinement to improve hydrogen borrowing by trapping the hydrogens atoms together with the catalysts and *in-situ* generated intermediates inside the mesoporous silica shells. We however found that trapping the intermediates is not enough to trigger the desired reactivity, as our system behaved optimally when the reaction space (*i.e.* the void between the alumina yolk and the silica shell) was mostly in the 6-16 nm range. Our results followed a volcano behaviour, with low activity at smaller yolk-shell gaps, maximum activity at the optimal gap size, and then decreased activity for particles that were over-etched and had lost the encapsulating silica layer. To the best of our knowledge, this is the first study of a confined hydrogen borrowing system, and we foresee confined systems playing a major role in the near future not only in hydrogen borrowing reactions but also in cascade systems in general that can benefit from the trapping of labile intermediates.

Experimental

All chemicals used in this work were acquired from Sigma Aldrich and used as received unless specified.

Synthesis of catalysts

The synthesis of our catalysts consists of 6 steps, according to the scheme in Figure 1. The steps are: 1) modification of Al_2O_3 with $Ru(OH)_x$, 2) templating, 3) silica coating, 4) surface protection, 5) etching with base, and 6) pyrolysis. We started from aluminum oxide NanoArc® AL-0405 99.5% (40-50 nm) acquired from Alfa Aesar as the core of our design. The alumina modification protocol was adapted from Mizuno and co-workers.[14] First (step 1), we calcinated alumina NPs in a tube furnace, ramping to 550 °C at 8.75 °C min^{-1} and holding at 550 °C for 3 h. Then, calcinated Al_2O_3 (4.0 g) was dispersed in DI water (200 mL) and sonicated with a probe at 20% amplitude for 5 min. In a separate container, we prepared a solution of $RuCl_3.3H_2O$ (0.5 mmol, 103.6 mg) in DI water (50 mL) which was also sonicated with a probe at 20% amplitude for 5 min. We then combined the $RuCl_3$ with the suspension of alumina NPs and set it magnetically stir at 1000 rpm. With the aid of a pHmeter, the suspension was titrated with NaOH (1 mol L^{-1}) until pH 13.2. The initial pH of the suspensions was around 2.5 and the volume of base needed for the titration varied from 15 to 20 mL across different batches. The alkaline suspension was then stirred for 18h and then centrifuged. The resulting dark gray powder was redispersed in DI water (50 mL) and dialyzed for 48 h. After dialysis, the suspension was centrifugated (supernatant pH 6.5) and either redispersed in DI water (40 mL) for further modification or lyophilized to give a dark gray powder, labeled $Al_2O_3/Ru(OH)_x$. The next steps in the synthesis were adapted from the methodology of Yin and co-workers.[25, 26] For templating (step 2), we prepared a solution containing 2.0 g of polyvinyl pyrrolidine (PVP) of molecular weight 55,000 in DI water (20 mL) and added to it a quarter of the previously prepared $Al_2O_3/Ru(OH)_x$ suspension (10 mL). The suspension was sonicated with a probe at 20% amplitude for 5 min and refluxed for 3 h. After cooling down, the product was washed by centrifugation with DI water (4 x 40 mL) to remove the excess PVP 55k and resuspended in DI water (15 mL). For silica coating (step 3), the prepared suspension of $Al_2O_3/Ru(OH)_x@PVP55$ was added to a 1 L RBF containing anhydrous ethanol (500 mL), DI water (10 mL), and ammonium hydroxide 28-30% (25 mL). We set the suspension to stir magnetically at 1000 rpm and added 5.0 mL of tetraethyl orthosilicate (TEOS). We left the suspension to stir for 18h, collected the silica-coated material $Al_2O_3/Ru(OH)_x@PVP55@SiO_2$ by centrifugation, and washed it once by centrifugation with DI water (40 mL). This is material E0, the non-etched catalyst. For surface protection (step 4), we prepared a solution containing 10.0 g of PVP 10,000 (*i.e.* PVP K15, purchased from Alfa Aesar) in DI water (200 mL). We then suspended the prepared material $Al_2O_3/Ru(OH)_x@PVP55@SiO_2$ in the PVP 10K solution and refluxed the suspension for 3 h. Moving to silica etching (step 5), once the suspension cooled down, we added to it a freshly-prepared solution of NaOH (1.5 g, micro-pearls acquired from Acros Organics) in DI water (5-10 mL). The alkaline suspension was stirred for various times (2-6 h) and then collected and washed once with DI water (40 mL) by centrifugation, redispersed in DI water (50 mL), and dialyzed for 48 h. After dialysis, the suspension was centrifugated (supernatant pH 6.5) and lyophilized to give a gray powder, labeled $Al_2O_3/Ru(OH)_x@PVP55@SiO_2$ EX (X = 2-6, the etching time in hours). Finally, the powders were then pyrolyzed (step 6) in a tube furnace under argon flow, ramping to 550 °C at 1 °C min^{-1} and holding at 550 °C for 5 h. The resulting materials are the final etched and pyrolyzed catalysts used in this work, labeled $Al_2O_3/Ru(OH)_x@PVP55@SiO_2$ EXP (X = 2-6, the etching time in hours). The non-etched material E0 was also pyrolyzed, giving material E0P.

Characterization of the catalysts

The Ru content on sample $Al_2O_3/Ru(OH)_x$ was measured by inductively coupled plasma atomic emission spectroscopy (ICP-OES) on a Thermo iCap 6500 Duo Series Spectrometer. We digested the samples (around 10 mg, triplicate) suspending them in a mixture of concentrated HCl (3 mL) and HF (2 mL) in XP-1500 vessels and leaving them at RT for 30 min; then we introduced the sealed vessels in a microwave digestion system programmed to reach 180 °C in 20 min and hold for 10 min at 600 W. We carried out X-Ray photoelectron spectroscopy (XPS) on samples $Al_2O_3/Ru(OH)_x$, $Al_2O_3/Ru(OH)_x$ pyrolyzed, and E5P on a Fischer Scientific Kα X-Ray spectrometer with an excitation source of Al Kα= 1486.6 eV. The binding energies were corrected by referencing the C 1s line to 284.80 eV. The spot size was 200 µm, running 5 survey scans at 200 mV for 50 ms residence times. Specific energy regions analyzed were Al 2p (5 scans, 85-65 eV), O 1s (3 scans, 545-525 eV), and overlapping C 1s and Ru 3d combined (10 scans, 298-276 eV), also at residence times of 50 ms. Deconvolution and peak positionS were determined using the CasaXPS software. We analyzed all samples by transmission electron microscopy (TEM) by deposing DI water suspensions onto a Cu grid with a carbon backing (Electron Microscopy Sciences). They were analyzed on a Thermo Scientific Talos F200X S/TEM operated at 200 keV, with high brightness XFEG Schottky source. Electron-dispersive X-ray spectroscopy (EDAX) was carried out with a SuperX G2 energy dispersive spectroscopy detector comprising four windowless SSDs, with a dwell time of 2 µs per scan for 20 min and a current probe of 500 pA. Data were processed using the software Velox®. Electron tomography was carried out using two STEM detectors: High angle annular dark field (HAADF) detector with a camera length of 200 mm. The datasets were obtained using the software SerialEM[34] and a tilt range of ±60°

with a tilt step of 2°. The 3D reconstruction was performed using the software IMOD[35] with a SIRT algorithm with 10 iterations. The visualization and manipulation of the 3D volume tomography were done using UCSF software Chimera.[36] Thermogravimetric analysis (TGA) was carried out on a TA Instruments Q50 machine, sample weight 5-10 mg, heating from RT to 1000 °C at 20 °C min^{-1}, with N_2 flow at the beginning at air flow after 800 °C. N_2-sorption isotherms were measured on a Quantachrome instrument and used to determine porosity (density-functional theory, DFT), and surface area (Brunauer-Emmett-Teller, BET). Statistical analysis of yolk-shell voids was done by manually measuring about 100-200 voids with clearly identifiable limits in bright-field TEM images (8-17 micrographs in total depending on the sample); the measurements were done using ImageJ (Figure S11). Measurement of the silica shell thickness were carried out similarly, over 100-300 particles (Figure S4). Counting of shell-free particles was carried out using the ImageJ counting tool measuring 400-600 clearly identifiable particles over 4-8 bright-field TEM images, depending on sample (Figure S5).

Catalysis

All chemicals involved in the catalytic tests were stored over molecular sieves 3 Å. In a typical experiment, we added aniline (around 0.25 mmol), benzyl alcohol (0.38 mmol), catalyst (100 mg), and solvent mesitylene (6 mL) in an Anton-Paar microwave vial. The reaction mixture was bubbled with argon for 15 min, then sealed and sonicated for 5 min. We then set the vials in an oil bath at 135 °C and magnetic stirring at 1600 rpm. After 18 h, we placed the vials in ice to quench the reaction, centrifuged the contents, washed them out with acetone (2 x 10 mL), filtered the product with celite, added the external standard 1,4-dimethoxybenzene (500 µL of a 0.41 mol L-1 solution in acetone), and completed the volume to 25.00 mL. The crude was analyzed on an Agilent 7890A gas chromatographer equipped with a flame ionization detector (GC-FID) and an HP-5ms 30 m x 250 µm, 0.25 µm film; the yields of the two main products N,1-diphenylmethanimine and N-benzylaniline were followed using a calibration curve built with the purchased pure products and the external standard. The H_2 released from reactions catalyzed by $Al_2O_3/Ru(OH)_x$ and E4P were analyzed by injecting 100 µL of the headspace of the sealed vials after 18 h of reaction in an Agilent 6890N gas chromatographer equipped with a thermal conductivity detector (GC-TDC) and using argon as the carrier gas; we used two columns (HP-Plot Q 30 m x 530 µm, 40.0 µm and HP Molsieve 5Å, 30 m x 530 µm, 25.0 µm) that were valve-switched after 11 min; splitless inlet at 200 °C, detector at 250 °C; oven held at 30 °C for 9 min, then ramped at 50 °C min^{-1} to 120 °C and held for 8 min.

ASSOCIATED CONTENT

Alumina NPs sizing; additional TEM images of confined materials pre-pyrolysis; measurement of the thickness of the silica shells; counting of coated and uncoated particles; X-Ray Photoelectron Spectroscopy (XPS); TEM images of non-confined materials; thermogravimetric analysis (TGA); nanotomography; catalysis results; pore volume and surface area; measurements of yolk-shell voids; pore-size distribution pre-etching; H_2 detection. This material is available along with the article.

AUTHOR INFORMATION

Corresponding Author

* audrey.moores@mcgill.ca

Author Contributions

All authors have given approval to the final version of the manuscript.

Funding Sources

We thank the Natural Science and Engineering Research Council of Canada (NSERC) - Discovery Grant and Discovery Accelerator Supplement, the Canada Foundation for Innovation (CFI), the McGill Sustainability Systems Initiative (MSSI), the Fonds de Recherche du Québec – Nature et Technologies (FRQNT) - Equipe program, the Centre for Green Chemistry and Catalysis (CGCC), and McGill University for their financial support.

ACKNOWLEDGMENTS

We are grateful to Ranjan Roy for the help with digestion and ICP-OES analysis, and Andrew Golsztajn for the help with GC-TCD analysis.

ABBREVIATIONS

Cp: cyclopentadienyl; phen: 1,10-phenanthroline; NP: nanoparticle; DFT: density-functional theory; MCM: Mobil composite material; PVP: polyvinyl pyrrolidone; $Al_2O_3/Ru(OH)_x$: alumina-supported ruthenium hydroxide; PDI: polydispersity index; $Al_2O_3/Ru(OH)_x$ @$pSiO_2$: alumina-supported ruthenium hydroxide yolk inside a porous silica shell; EX (X = 0, 2, 3 ,4 ,5, 6): $Al_2O_3/Ru(OH)_x$ @$pSiO_2$ etched for X hours in NaOH; EXP (X = 0, 2, 3 ,4 ,5, 6): $Al_2O_3/Ru(OH)_x$ @$pSiO_2$ etched for X hours in NaOH and pyrolyzed; ICP-OES: inductive coupled plasma optical transmission spectroscopy; XPS: X-ray photoelectron spectroscopy; TGA: thermogravimetric analysis; TEM: transmission electron microscopy; BET: Brunauer, Emmett, and Teller; EDAX: energy-dispersive X-ray analysis; HAADF: high-angular annular dark-field; GC-TCD: gas chromatography with a thermal conductivity detector; GC-FID: gas chromatography with a flame ionization detector.

REFERENCES

1. Vile, G.; Albani, D.; Almora-Barrios, N.; Lopez, N.; Perez-Ramirez, J., Advances in the Design of Nanostructured Catalysts for Selective Hydrogenation. *ChemCatChem* **2016,** *8* (1), 21-33.
2. Wang, D.; Astruc, D., The Golden Age of Transfer Hydrogenation. *Chem. Rev.* **2015,** *115* (13), 6621-6686.
3. Gnanamgari, D.; Moores, A.; Rajaseelan, E.; Crabtree, R. H., Transfer hydrogenation of imines and alkenes and direct reductive amination of aldehydes catalyzed by triazole-derived iridium (I) carbene complexes. *Organometallics* **2007,** *26* (5), 1226-1230.
4. Corma, A.; Navas, J.; Sabater, M. J., Advances in One-Pot Synthesis through Borrowing Hydrogen Catalysis. *Chem. Rev.* **2018,** *118* (4), 1410-1459.
5. Reed-Berendt, B. G.; Latham, D. E.; Dambatta, M. B.; Morrill, L. C., Borrowing Hydrogen for Organic Synthesis. *ACS Cent. Sci.* **2021,** *7* (4), 570-585.
6. Bahn, S.; Imm, S.; Neubert, L.; Zhang, M.; Neumann, H.; Beller, M., The Catalytic Amination of Alcohols. *ChemCatChem* **2011,** *3* (12), 1853-1864.

7. Grigg, R.; Mitchell, T. R. B.; Sutthivaiyakit, S.; Tongpenyai, N., Transition Metal-Catalyzed N-Alkylation of Amines by Alcohols. *J. Chem. Soc., Chem. Commun.* **1981,** (12), 611-612.
8. Watanabe, Y.; Tsuji, Y.; Ohsugi, Y., The Ruthenium Catalyzed N-Alkylation and N-Heterocyclization of Aniline Using Alcohols and Aldehydes. *Tetrahedron Lett.* **1981,** *22* (28), 2667-2670.
9. Reed-Berendt, B. G.; Polidano, K.; Morrill, L. C., Recent advances in homogeneous borrowing hydrogen catalysis using earth-abundant first row transition metals. *Org. Biomol. Chem.* **2019,** *17* (7), 1595-1607.
10. Fujita, K.; Li, Z. Z.; Ozeki, N.; Yamaguchi, R., N-Alkylation of amines with alcohols catalyzed by a Cp*Ir complex. *Tetrahedron Lett.* **2003,** *44* (13), 2687-2690.
11. bBalcells, D.; Nova, A.; Clot, E.; Gnanamgari, D.; Crabtree, R. H.; Eisenstein, O., Mechanism of homogeneous iridium-catalyzed alkylation of amines with alcohols from a DFT study. *Organometallics* **2008,** *27* (11), 2529-2535.
12. Guo, B.; Li, H. X.; Zhang, S. Q.; Young, D. J.; Lang, J. P., C-N Bond Formation Catalyzed by Ruthenium Nanoparticles Supported on N-Doped Carbon via Acceptorless Dehydrogenation to Secondary Amines, Imines, Benzimidazoles and Quinoxalines. *ChemCatChem* **2018,** *10* (24), 5627-5636.
13. Anastas, P.; Eghbali, N., Green Chemistry: Principles and Practice. *Chem. Soc. Rev.* **2010,** *39* (1), 301-312.
14. Kim, J. W.; Yamaguchi, K.; Mizuno, N., Heterogeneously catalyzed selective N-alkylation of aromatic and heteroaromatic amines with alcohols by a supported ruthenium hydroxide. *J. Catal.* **2009,** *263* (1), 205-208.
15. Li, A. Y.; Dumaresq, N.; Segalla, A.; Braidy, N.; Moores, A., Plasma-made (Ni0.5Cu0.5)Fe2O4 Nanoparticles for Alcohol Amination under Microwave Heating. *ChemCatChem* **2019,** *11* (16), 3959-3972.
16. Trinh, T. K. H.; de Hemptinne, J. C.; Lugo, R.; Ferrando, N.; Passarello, J. P., Hydrogen Solubility in Hydrocarbon and Oxygenated Organic Compounds. *Journal of Chemical and Engineering Data* **2016,** *61* (1), 19-34.
17. Nova, A.; Balcells, D.; Schley, N. D.; Dobereiner, G. E.; Crabtree, R. H.; Eisenstein, O., An Experimental-Theoretical Study of the Factors That Affect the Switch between Ruthenium-Catalyzed Dehydrogenative Amide Formation versus Amine Alkylation. *Organometallics* **2010,** *29* (23), 6548-6558.
18. Mattey, A. P.; Ford, G. J.; Citoler, J.; Baldwin, C.; Marshall, J. R.; Palmer, R. B.; Thompson, M.; Turner, N. J.; Cosgrove, S. C.; Flitsch, S. L., Development of continuous flow systems to access secondary amines through previously incompatible biocatalytic cascades. *Angew. Chem. Int. Ed.* **2021,** *60* (34), 18660-18665.
19. Prieto, G.; Tuysuz, H.; Duyckaerts, N.; Knossalla, J.; Wang, G. H.; Schuth, F., Hollow Nano- and Microstructures as Catalysts. *Chem Rev* **2016,** *116* (22), 14056-14119.
20. Wu, S. M.; Yang, X. Y.; Janiak, C., Confinement Effects in Zeolite-Confined Noble Metals. *Angew. Chem. Int. Ed.* **2019,** *58* (36), 12340-12354.
21. Dong, B.; Pei, Y. C.; Zhao, F.; Goh, T. W.; Qi, Z. Y.; Xiao, C. X.; Chen, K. C.; Huang, W. Y.; Fang, N., In situ quantitative single-molecule study of dynamic catalytic processes in nanoconfinement. *Nat. Catal.* **2018,** *1* (2), 135-140.
22. Dong, B.; Pei, Y. C.; Mansour, N.; Lu, X. M.; Yang, K.; Huang, W. Y.; Fang, N., Deciphering nanoconfinement effects on molecular orientation and reaction intermediate by single molecule imaging. *Nat. Commun.* **2019,** *10*.
23. Terra, J. C. S.; Moores, A.; Moura, F. C. C., Amine-Functionalized Mesoporous Silica as a Support for on-Demand Release of Copper in the A(3)-Coupling Reaction: Ultralow Concentration Catalysis and Confinement Effect. *ACS Sustain. Chem. Eng.* **2019,** *7* (9), 8696-8705.
24. Terra, J. C. S.; Martins, A. R.; Moura, F. C. C.; Weber, C. C.; Moores, A., Making more with less: confinement effects for more sustainable chemical transformations. *Green Chem.* **2022,** *24* (4), 1404-1438.
25. Zhang, Q.; Ge, J. P.; Goebl, J.; Hu, Y. X.; Lu, Z. D.; Yin, Y. D., Rattle-Type Silica Colloidal Particles Prepared by a Surface-Protected Etching Process. *Nano Res.* **2009,** *2* (7), 583-591.
26. Zhang, Q.; Zhang, T. R.; Ge, J. P.; Yin, Y. D., Permeable silica shell through surface-protected etching. *Nano Lett.* **2008,** *8* (9), 2867-2871.
27. Morgan, D. J., Resolving ruthenium: XPS studies of common ruthenium materials. *Surf. Interface Anal.* **2015,** *47* (11), 1072-1079.
28. Liu, J.; Qiao, S. Z.; Budi Hartono, S.; Lu, G. Q., Monodisperse yolk–shell nanoparticles with a hierarchical porous structure for delivery vehicles and nanoreactors. *Angew. Chem. Int. Ed.* **2010,** *49* (29), 4981-4985.
29. Teng, Z.; Zhang, J.; Li, W.; Zheng, Y.; Su, X.; Tang, Y.; Dang, M.; Tian, Y.; Yuwen, L.; Weng, L., Facile Synthesis of Yolk–Shell-Structured Triple-Hybridized Periodic Mesoporous Organosilica Nanoparticles for Biomedicine. *Small* **2016,** *12* (26), 3550-3558.
30. Yang, T.; Zhou, R.; Wang, D.-W.; Yamauchi, Y.; Qiao, S. Z.; Monteiro, M. J.; Liu, J., Hierarchical mesoporous yolk–shell structured carbonaceous nanospheres for high performance electrochemical capacitive energy storage. *Chem. Commun.* **2015,** *51* (13), 2518-2521.
31. Krishna, R., Diffusion in porous crystalline materials. *Chem. Soc. Rev.* **2012,** *41* (8), 3099-3118.
32. Paunović, V.; Pérez-Ramírez, J., Catalytic halogenation of methane: a dream reaction with practical scope? *Catal. Sci. Technol.* **2019,** *9* (17), 4515-4530.
33. Xiao, J.; Pan, X.; Zhang, F.; Li, H.; Bao, X., Size-dependence of carbon nanotube confinement in catalysis. *Chem. Sci.* **2017,** *8* (1), 278-283.
34. Mastronarde, D. N., SerialEM: a program for automated tilt series acquisition on Tecnai microscopes using prediction of specimen position. *Microscopy and Microanalysis* **2003,** *9* (S02), 1182-1183.
35. Kremer, J. R.; Mastronarde, D. N.; McIntosh, J. R., Computer visualization of three-dimensional image data using IMOD. *Journal of structural biology* **1996,** *116* (1), 71-76.
36. Pettersen, E. F.; Goddard, T. D.; Huang, C. C.; Couch, G. S.; Greenblatt, D. M.; Meng, E. C.; Ferrin, T. E., UCSF Chimera—a visualization system for exploratory research and analysis. *Journal of computational chemistry* **2004,** *25* (13), 1605-1612.